Biophysical *Journal*
Article

Biophysical Society

# Synaptotagmin-1 and Doc2b Exhibit Distinct Membrane-Remodeling Mechanisms

Raya Sorkin,[1,2,3] Margherita Marchetti,[1,2] Emma Logtenberg,[4] Melissa C. Piontek,[2] Emma Kerklingh,[1] Guy Brand,[1] Rashmi Voleti,[5] Josep Rizo,[5] Wouter H. Roos,[2] Alexander J. Groffen,[4] and Gijs J. L. Wuite[1,*]

[1]Department of Physics and Astronomy and LaserLab, Vrije Universiteit Amsterdam, Amsterdam, the Netherlands; [2]Department of Molecular Biophysics, Zernike Instituut, Rijksuniversiteit Groningen, Groningen, the Netherlands; [3]Raymond & Beverly Sackler School of Chemistry, Tel Aviv University, Tel Aviv, Israel; [4]Department of Functional Genomics and Clinical Genetics, Vrije Universiteit and VU Medical Center Amsterdam, Amsterdam, the Netherlands; and [5]Departments of Biophysics, Biochemistry, and Pharmacology, UT Southwestern Medical Center, Dallas, Texas

ABSTRACT Synaptotagmin-1 (Syt1) is a calcium sensor protein that is critical for neurotransmission and is therefore extensively studied. Here, we use pairs of optically trapped beads coated with SNARE-free synthetic membranes to investigate Syt1-induced membrane remodeling. This activity is compared with that of Doc2b, which contains a conserved $C_2AB$ domain and induces membrane tethering and hemifusion in this cell-free model. We find that the soluble $C_2AB$ domain of Syt1 strongly affects the probability and strength of membrane-membrane interactions in a strictly $Ca^{2+}$- and protein-dependent manner. Single-membrane loading of Syt1 yielded the highest probability and force of membrane interactions, whereas in contrast, Doc2b was more effective after loading both membranes. A lipid-mixing assay with confocal imaging reveals that both Syt1 and Doc2b are able to induce hemifusion; however, significantly higher Syt1 concentrations are required. Consistently, both $C_2AB$ fragments cause a reduction in the membrane-bending modulus, as measured by a method based on atomic force microscopy. This lowering of the energy required for membrane deformation may contribute to $Ca^{2+}$-induced fusion.

SIGNIFICANCE In this work, we used optical tweezers in combination with confocal fluorescence microscopy, as well as atomic force microscopy (AFM), to explore membrane remodeling by calcium sensor proteins that are regulators of synaptic vesicle fusion. Our results clearly show that Synaptotagmin-1 (Syt1) binds significantly more strongly to membranes than to other Syt1 molecules, thus resolving a long-standing controversy in the field for the mode of Syt1 action during fusion. Furthermore, using AFM nanoindentation, we succeeded in quantitatively and directly demonstrating that the binding of Syt1 and Doc2b to membranes results in membrane softening. This lowering of the energy required for membrane deformation possibly contributes to fusion facilitation by calcium sensor proteins and may be a general feature of $C_2AB$ domains.

## INTRODUCTION

$Ca^{2+}$ sensor proteins tightly control the secretion of neurotransmitters and endocrine substances. After the arrival of an action potential to the synaptic terminal, $Ca^{2+}$ influx triggers the fast fusion of synaptic vesicles with the presynaptic plasma membrane. This process depends on SNAREs, Munc18-1, Munc13s, complexins, and $Ca^{2+}$ sensor proteins such as Synaptotagmin-1 (Syt1), among other proteins (1). Syt1 contains a single transmembrane domain and two cytoplasmic $C_2$ domains (together named $C_2AB$). The $C_2A$ and $C_2B$ domains can bind three and two $Ca^{2+}$ ions, respectively, accompanied by binding to phosphatidylserine (PS) in the membrane (2). The $C_2AB$ domain also binds to phosphatidylinositol 4,5-bisphosphate ($PIP_2$), SNARE proteins, and complexin (3–6). $Ca^{2+}$ binding is thought to be the direct trigger for vesicle fusion (1,2,7).

Despite extensive research, the exact role of Syt1 in membrane fusion and, in particular, its membrane-bound configuration before and during fusion remains uncertain. Several mechanisms have been suggested, which are recently reviewed by Park et al. (8). The "clamping hypothesis," for example, proposes that Syt1 (together with complexin)

*Submitted July 15, 2019, and accepted for publication December 16, 2019.*

*Correspondence: gwuite@nat.vu.nl

Raya Sorkin and Margherita Marchetti contributed equally to this work.

Alexander J. Groffen and Gijs J. L. Wuite are senior authors.

Editor: Sarah Veatch.

https://doi.org/10.1016/j.bpj.2019.12.021

prevents fusion in the absence of a $Ca^{2+}$ signal (9). Syt1 is also proposed to bring the vesicle and plasma membranes into close proximity upon $Ca^{2+}$ binding, thus assisting fusion (10,11). The $C_2AB$ domain of Syt1 was demonstrated to directly bridge the membranes through simultaneous binding of the $Ca^{2+}$-binding loops and other regions of the $C_2B$ domain, which is coined the "direct bridging mechanism" (11,12). These other regions may involve conserved basic lysines (13–15) (K326 and K327) and, although debated, two conserved arginines (11,16) (R398 and R399). It was also demonstrated that upon $Ca^{2+}$ binding, the $Ca^{2+}$-binding loops not only associate with but also insert into the membrane (17–19). This insertion penetrates one leaflet of the membrane to approximately the depth of lipid glycerol backbones (7,20), thereby inducing local membrane curvature (21–23) and acyl chain disorder (24). Full membrane fusion is associated with complete SNARE complex assembly, leading to pore formation and release of the vesicle cargo, whereas Syt1 also contributes to pore expansion (25–27). Two other studies led to another possible mechanism involving the interaction of protein oligomers bound on both membranes, the so-called oligomerization mechanism (28,29), although such oligomerization may arise because of insufficient purification of the soluble Syt1 fragment used (12). Nevertheless, very recent work proposed a different mechanism according to which synaptotagmins form ring-like oligomers that facilitate vesicle docking, whereas their disassembly, coupled to $Ca^{2+}$ influx, triggers SNARE-driven fusion (30–32). There is also evidence that Syt1-SNARE interactions are critical for neurotransmitter release, although the relevant binding mode(s) are still under debate (3–5). In summary, despite the wealth of information available, the mechanisms by which Syt1 and other $Ca^{2+}$ sensor proteins facilitate membrane fusion remain unclear.

Single-site mutations in the $C_2AB$ domain of Syt1 may affect both protein and phospholipid interactions, making it particularly challenging to clearly dissect their contribution to membrane remodeling. Direct effects of Syt1-$C_2AB$ on membranes have been observed in cell-free liposome preparations in which 10 $\mu$M of the protein induced tubules with an outer diameter of 17.3 $\pm$ 3 nm (22). Membranes were negatively stained for electron microscopy with uranyl acetate, a reagent that strongly perturbs membranes (33), prompting the question of whether membrane curvature is similarly affected in the absence of this reagent. Similar tubulation has also been reported for Doc2b (34), another double C2-domain-containing protein that is widely expressed and contains a $C_2AB$ domain with high structural similarity to that of Syt1 (35,36). Like Syt1, Doc2b similarly interacts with membranes (via PS and $PIP_2$) and SNARE proteins to trigger fusion (34,37). In contrast to Syt1, Doc2b is a soluble cytoplasmic protein that lacks a transmembrane domain. During cellular activity, Doc2b associates reversibly with the plasma membrane in neurons, chromaffin cells, and other cell types (38). Two modes of membrane recruitment were identified. First, diacylglycerol activation of the C1 domain in Munc13 causes a cotranslocation of Doc2b (39). This pathway requires a Munc13-interacting domain located in the N-terminal domain outside the $C_2AB$ motif. Second, $Ca^{2+}$ directly activates the $C_2AB$ domain and causes its PS-dependent association with the inner membrane leaflet (35). Doc2b appears to have a higher $Ca^{2+}$ affinity than Syt1 (40). In neurons, Syt1 and Doc2b each contribute to synaptic vesicle secretion but exhibit very distinct kinetics: Syt1 triggers fast synchronous neurotransmission evoked by action potentials and the subsequent opening of voltage-gated $Ca^{2+}$ channels (41), whereas Doc2b contributes to the so-called spontaneous release events that occur in the absence of action potentials (34). In addition, Doc2b is also implicated in the secretion of chromaffin granules (37,42) and insulin (43) and the externalization of glucose transporters (44,45).

Recently, we designed a method using pairs of optically trapped beads coated with synthetic membranes with which we can study the protein-induced membrane-membrane interactions (46). Here, we apply this method to investigate the dynamics and mechanics of the canonical $Ca^{2+}$ sensor Syt1 as well as Doc2b-induced membrane interactions, revealing differences in membrane interactions of the two $Ca^{2+}$ sensor proteins. Using atomic force microscopy (AFM) nanoindentation experiments, we further provide the first direct quantitative evidence that $C_2AB$ domains have a profound mechanical effect on the membranes they attach to and that the extent of this effect differs between the proteins. Together, our study provides important new insights into how calcium sensor $C_2AB$ domains may affect membrane fusion.

## MATERIALS AND METHODS

### Bead coating

1,2-Dioleoyl-sn-glycero-3-phosphocholine (DOPC); 1,2-dioleoyl-sn-glycero-3-phospho-L-serine (DOPS); and 1-stearoyl-2-arachidonoyl-sn-glycero-3-phospho-1′-myo-inositol-4′,5′-bisphosphate were purchased from Avanti Polar Lipids (Alabaster, Alabama). Lissamine-Rhodamine B 1,2-dihexadecanoyl-sn-glycero-3-phosphoethanolamine was purchased from Invitrogen (Carlsbad, California). To prepare membrane-coated microspheres, polystyrene nonporous beads (diameter 3.84 $\mu$m $\pm$ 4%) were acquired from Spherotech (Lake Forest, Illinois). Before the coating procedure, the beads were washed three times in Milli-Q and collected after each wash by centrifugation for 3 min at 900 $\times$ $g$. Liposomes were prepared by mixing lipids in chloroform solutions, extensively drying the mix under a nitrogen gas stream, and hydrating the lipid cake in Milli-Q to a final lipid concentration of 1 mg/mL. The suspension was then vortexed, sonicated in ice water, and centrifuged for 90 min at 21,000 $\times$ $g$ at 4°C. The supernatant was mixed with beads and incubated for 16 h at 4°C in the presence of 3 mM $CaCl_2$ with gentle continuous rotation to keep the beads dispersed. The beads were washed (each time collecting the beads for 3 min at 900 $\times$ $g$ and gently resuspending them) in buffer 1 (25 mM HEPES, pH 7.4, 200 mM NaCl, 1 mM Tris 2-carboxyethyl-phosphine (TCEP), and

5 mM EDTA), then buffer 2 (25 mM HEPES, pH 7.4, 100 mM NaCl, 1 mM TCEP, and 0.25 mM $CaCl_2$), and then twice in buffer 3 (25 mM HEPES, pH 7.4, 25 mM NaCl, 1 mM TCEP, and 0.25 mM $CaCl_2$). The coated beads were stored at 4°C before use. To visualize lipid tethers that formed in the presence of Syt1-$C_2$AB or Doc2b-$C_2$AB, we prepared coated beads containing 1% Rhodamine-phosphatidylethanolamine (PE). We note that the membranes are loose and not tightly attached to the beads (as can be seen in the electron microscopy images in our previous work (46)); therefore, membrane tension should be very low.

## Recombinant proteins

Recombinant Doc2b-$C_2$AB (rat, amino acid residues 115–412) was prepared as previously described (46). Recombinant Syt1-$C_2$AB (rat, amino acid residues 140–421) or Syt1-$C_2$AB-mCherry (same fragment) were cloned into the pGEX4T3 vector and transformed into the *E. coli* BL21 strain for expression. Cultures were grown in luria broth medium (VWR Life Science, Radnor, Pennsylvania) enriched with 100 $\mu$g/mL ampicillin (Fisher bioreagents, Pittsburgh, Pennsylvania). Gene expression was induced with 0.1 mM isopropyl $\beta$-d-1-thiogalactopyranoside (Fisher bioreagents, Pittburgh, Pennsylvania), after which cultures were grown overnight at 34°C and 210 rpm to maximize aeration. Lysate buffer (300 mM NaCl, 50 mM Tris, pH 7.5, 10 mM EDTA, 1 mg/mL lysozyme, protease inhibitor cocktail) was added to the bacterial pellet before the lysate was sonicated four times for 15 s with 1-min intervals while cooling on ice water. Pellet was incubated for 2 h with 1% triton-X100 and then centrifuged for 30 min at 8500 $\times$ $g$ to dispose of any insoluble bacterial lysate. Protein purification took place by means of glutathione agarose bead (Sigma-Aldrich, St. Louis, Missouri) affinity assay. Glutathione agarose bead slurry was added to the lysate and incubated O/N at 4°C and 5 rpm. Afterward, beads were washed with high-salt buffer (300 mM NaCl, 50 mM Tris, pH 7.4, 10 mM EDTA) and loaded into a disposable column. After a wash with 150 mM NaCl, 50 mM Tris, pH 7.4, 1.4 mM $MgCl_2$, the column was incubated with DNase I (50 U/mL; Roche Diagnostics, Basel, Switzerland) and RNase A (50 U/mL; Invitrogen, Carlsbad, California) for 15 min at room temperature. The column was washed with low-salt buffer (150 mM NaCl, 50 mM Tris, pH 7.4). Protein was cleaved from the glutathione agarose beads by incubation with thrombin (SERVA Electrophoresis, Heidelberg, Germany) at 4°C. Protein concentration was determined with sodium dodecyl sulfate polyacrylamide-gel electrophoresis stained with SYPRO ruby using known quantities of bovine serum albumin for calibration. The SYPRO ruby signal was visualized with a scan performed by the Fuji5000. For key experiments, Syt1-$C_2$AB was $^{15}$N-labeled by expressing the protein in minimal medium containing $^{15}NH_4Cl$ as the sole nitrogen source, and the protein was purified by gel filtration and ion exchange chromatography as described (10). $^1$H-$^{15}$N heteronuclear single quantum coherence spectra of the protein were then used to verify the absence of polyacidic contaminants that are difficult to remove from Syt1 fragments containing the $C_2$B domain (47). These key experiments included the AFM measurements and the comparison between symmetric and asymmetric protein binding to membrane-coated beads. Proteins were aliquoted and stored at −80°C until use.

## Optical tweezers

We use a C-trap confocal fluorescence optical tweezers setup (LUMICKS) made of an inverted microscope based on a water-immersion objective (NA 1.27) together with a condenser top lens placed above the flow cell. The optical traps are generated by splitting a 1064-nm laser (10-W continuous wave fiber laser) into two orthogonally polarized, independently steerable optical traps. To steer the two traps, both one coarse-positioning piezo stepper mirror and one accurate piezo mirror were used. Optical traps were used to capture lipid-coated beads. The displacement of the trapped beads from the center of the trap was measured and converted into a force signal by back-focal plane interferometry of the condenser lens using two position-sensitive detectors. The beads' distance was determined by using template matching on the real-time imaging of a bright field movie of the trapped beads. The samples were illuminated by a bright field 875-nm LED and imaged in transmission onto a metal-oxide semiconductor (CMOS) camera.

## Confocal fluorescence microscopy

A single, pulsed laser system (ALP-745-710-SC, 20 MHz, 100-ps pulses; Fianium, Southhampton, United Kingdom) was used for confocal fluorescence excitation at a wavelength of 543 nm, selected from a supercontinuum spectrum by using an Acousto-Optic tunable filter (AOTF; AOTFnc-VIS-TN; AA Opto-Electronic, Orsay, France). For scanning, a fast tip/tilt piezo mirror (S-334.1SD, maximal scan rate 200 Hz; Physik Instrumente, Karlsruhe, Germany) was used. For confocal detection, the emitted fluorescence was descanned, separated from the excitation by a dichroic mirror (F33-554; AHF Analysentechnik, Tübingen, Germany), and filtered using an emission filter (F47-586; AHF Analysentechnik, Tübingen, Germany). Photons were counted using fiber-coupled avalanche photodiodes (APDs; SPCM-AQRH-14-FC, fibers SPCM-QC9; PerkinElmer, Waltham, Massachusetts). The multimode fibers (62 $\mu$m diameter) serve as pinholes that provide background rejection. Microfluidics: a 5-channel laminar flow cell (LUMICKS, Amsterdam, the Netherlands) was assembled onto an automated XY-stage (MS-2000; Applied Scientific Instrumentation, Eugene, Oregon). The latter allowed the controlled transfer in a highly efficient manner of the optically trapped beads through the channels of the flow cell, which contained the proteins of interest.

## Approach and separation routine

Repeated approach and separation of lipid-coated beads were performed as previously described (46). Briefly, one bead was kept stationary (the left trap, Fig. 1 *a*), and the other bead was moved toward and away from it (the $x$ dimension). We recorded the forces in $x$ and $y$ directions on both beads and used the force data in the $x$ direction of the stationary bead unless stated otherwise. At the initial separation of ~7 $\mu$m between the beads, the force on the stationary bead is zero. During an experiment, the beads were brought into contact such that a repulsive force of ~10 pN was exerted on the stationary bead (step with positive force in Fig. 1 *a*) and then separated. The contact time in such experiments was 5 s. If specific protein-dependent interactions occur, rupture forces are recorded upon separation, which are observed as negative force peaks (arrows in Fig. 1 *a* indicate rupture events). This procedure was repeated 20 times or until a bead escaped the trap because of very strong interactions upon pulling. The speed at which the bead is retracted is known to influence rupture forces. Therefore, a constant trap speed of 2 $\mu$m s$^{-1}$ was used in all experiments. The term "probability of interactions" throughout the text refers to the fraction of approach and separation events that resulted in the formation of a tether, as observed from the "negative" force peaks in Fig. 1 *b*. The threshold to distinguish a negative force peak from noise is described in Brouwer et al. (46). The "positive" force in this plot denotes the force during bead approach and a slight push into contact. We kept this force roughly constant, at 20–25 pN, to avoid possible effects of this force on the forces recorded during separation of the beads.

## Protein concentrations

The physiologically relevant protein concentrations previously estimated in synaptic boutons are ~70 $\mu$M for Syt1 and ~25 $\mu$M for Doc2b (48). Protein concentrations used in our study were always lower and were chosen based on experimental needs. When measuring tether break/unbinding forces, we tuned the concentration such that it was high enough to allow frequent events but not too high to keep the forces within the

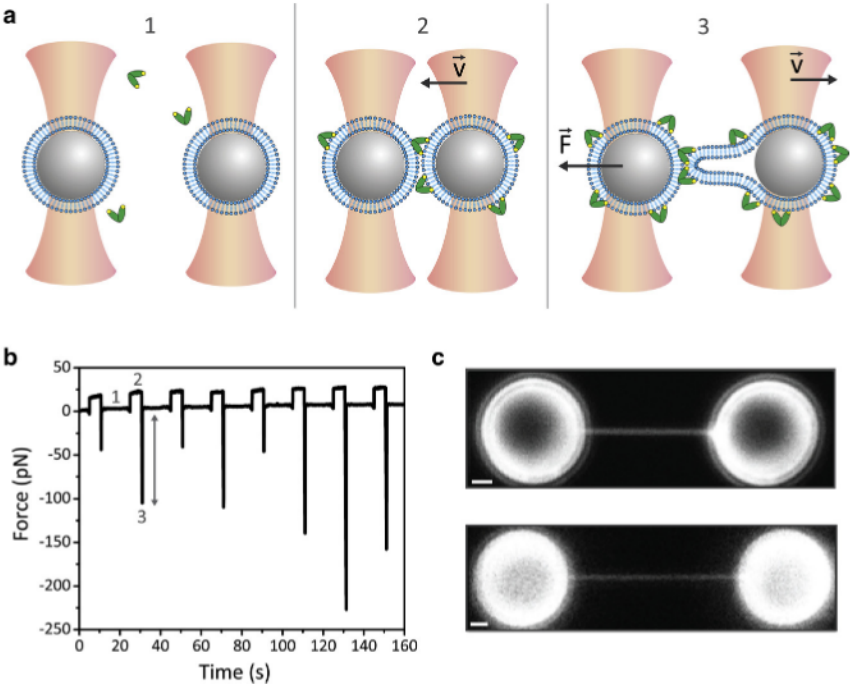


FIGURE 1 Membrane interactions captured with optical tweezers and confocal fluorescence microscopy. (*a*) A schematic (not to scale) of the dual-beam optical trapping setup used to manipulate two polystyrene microbeads (*gray*) coated with a phospholipid bilayer (*blue*) in the presence of proteins (*green*) and $Ca^{2+}$ ions (*yellow dots*) is shown in panel 1. The liposomes are brought into contact for 5 s (panel 2) and moved away (panel 3) with a constant velocity by an automated approach and separation method. The force on the left fixed trap is measured. (*b*) A typical force-time plot showing eight consecutive interactions is shown. The force is zero when the liposomes are apart (1). A positive force occurs during membrane contact (2), and a negative force occurs during bead separation (3), indicative of tether formation. The rupture force (indicated by a *gray arrow*) is used to quantify the strength of each tether. (*c*) Shown are confocal fluorescence images of membrane tethers visualized in the presence of labeled proteins (Syt1-$C_2$AB-mCherry, *top panel*) or labeled phospholipids (1% Rhodamine-PE, *bottom panel*) on both beads. Scale bars, 1 $\mu$m. To see this figure in color, go online.

experimental range. The maximal force we could apply with the optical trap, given our chosen beads, buffers, and laser power, was ~300 pN. If protein concentrations were too high, the measured force was limited by the force at which the beads escaped the optical trap. This led us to use concentrations of 0.1–0.5 $\mu$M for Syt1 and 0.05 $\mu$M for Doc2b in Figs. 3 and 4. To test whether hemifusion or full fusion had occurred by monitoring the change in fluorescence, we were no longer constrained by this limitation because there was no need to pull the beads far apart. Therefore, for the experiments described in Fig. 6 as well as AFM experiments in Fig. 7, concentrations higher and closer to physiological concentrations were used.

## Symmetric and asymmetric experiments

To test the effect of protein coating configuration on interaction strength and probability, experiments were performed as follows: beads were flushed into channel 1 containing buffer 3 without protein. After catching two beads, they were moved into the protein containing channel 4. After incubation in the protein channel for 10 s, the beads were moved into channel 3, which contained the same buffer without protein. Symmetrical measurements were then conducted directly in channel 3. For asymmetrical measurements, one of the beads was dropped, and a different nonprotein-coated bead was caught in channel 1. Then the beads were moved into the buffer-containing channel 3, and measurements were performed. The fluorescently labeled bead was protein coated in 50% of the cases, and the presence of the protein coating on either the labeled or unlabeled membrane did not have any effect on the results.

## Data acquisition and analysis

Data analysis was performed using custom written software in python (Gitlab link: https://gitlab.com/sorkin.raya/membrane-interactions-tweezers) to extract force data at a frequency of 100 Hz. To discriminate protein-mediated specific interactions from unspecific adhesion between the membranes, a force threshold of 25 pN was used throughout the analysis. Median rupture forces as presented in the figures were determined by bootstrapping with 1000 iterations, resampling 90% of the data. Error bars are standard deviation of the bootstrapped values.

## Liposome preparation for AFM

All lipid-chloroform solutions and cholesterol were purchased from Avanti Polar Lipids (Alabaster, Alabama). First, a round-bottom flask was cleaned with 96% ethanol and then washed two times with soap followed by rinsing two times with acetone. After that, the round-bottom flask was dried under argon flow for ~15 min. The lipids were mixed in the round-bottom flask (for spectrophotometer experiments: 50:20:30 (mole-%) DOPC:DOPS:cholesterol; for AFM experiments: 44% cholesterol, 20% porcine brain PS, 21% egg phosphatidylcholine (PC), and 15% egg sphingomyelin (SM)). The solvent was evaporated in a rotary evaporator at 100 mbar for 60 min and immersed in a water bath (40°C). After that, buffer was added to the dried lipid cake to attain a final lipid concentration of 1 mg/mL. Vortexing this mixture together with glass beads (4 mm diameter) supported the resuspension of the lipids. Subsequently, the resuspended lipids underwent five freeze and thaw cycles (each ~20 s in liquid nitrogen followed by 5 min in a water bath at 40°C) before the liposomes were extruded 31 times using a mini extruder from Avanti Polar Lipids (Alabaster, Alabama) and a 0.1-$\mu$m filter pore size. Before extrusion, the mini extruder and syringes were thoroughly cleaned by rinsing with water and 70% ethanol. The liposomes were stored in the fridge overnight and on ice throughout the measurements and used within 5 days.

## Liposome aggregation assay and analysis

The liposome aggregation assay was described in detail elsewhere (37). The spectrophotometer measurements were conducted with a Varian Cary 50 UV-Vis Spectrophotometer from Agilent Technologies (Santa Clara, California). For all measurements, a wavelength of 350 nm was used, the average reading was 0.1 s, and a cycle was set to 1.00 s. A precision cell (cuvette) made of Quartz SUPRASIL (light path 10.00 mm) from Hellma KG (Müllheim, Germany) was used to perform the experiments. The blank measurement was done for 500 s with 170 $\mu$L buffer 3 + 40 $\mu$L liposomes (DOPC:DOPS:cholesterol 50:20:30 (mole-%) at 1 mg/mL). Right before

each measurement, the cuvette was rinsed three times with buffer 3 and then loaded with 160 $\mu$L buffer 3 and 40 $\mu$L liposomes. The liposome dispersion was gently mixed twice by flipping the cuvette over. ~87 s after the starting time of the measurement, the cuvette was taken out of the spectrophotometer. At ~100 s of the measurement, 10 $\mu$L protein (titrated before) was added to one side of the precision cell and mixed twice by flipping the cuvette carefully to the injection side. Right after, the cuvette was inserted back into the spectrophotometer, and the absorbance measurement was continued for a total of 500 s. Before switching samples, the cuvette was cleaned by rinsing multiple times with buffer 3 and Milli-Q water and dried under a nitrogen flow.

All curves were baseline corrected: the average absorption before extracting the cuvette (first ~87 s) was calculated and subsequently subtracted from all absorbance data points of a measurement. After that, the average maximum absorbance (maximum liposome binding) and the corresponding SEM values were determined for each measurement condition, e.g., each protein concentration. At least three measurements per condition were performed.

## AFM experiments

Liposomes were adhered to poly-L-lysine-coated glass slides, which were prepared as follows: slides were cleaned in a 96% ethanol and 3% HCl solution for 10 min. Next, they were coated for 1 h in poly-L-lysine (0.001%; Sigma) solution, rinsed with ultrapure water, and dried for 20 h at 37°C. They were stored at 7°C for up to 1 month. Liposomes and proteins at the desired concentration were mixed in a tube and diluted in buffer 3, and then a 10 $\mu$L drop of the mixture was incubated on the glass slide. After a 5- to 10-min incubation, vesicles were imaged in PeakForce Tapping mode on a Bruker Bioscope catalyst setup. Imaging was performed at room temperature (22°C). Force set point during imaging was 100–200 pN. Nanoindentations were performed by first making an image of a single particle and then indenting it until a trigger force of 0.5 nN was reached and subsequently applying higher forces (2–10 nN) at a velocity of 250 nms$^{-1}$. Importantly, both before and after the vesicle indentation, the tip was checked for adherent lipid bilayers by recording a force-distance plot on the glass surface until a trigger force of 5 nN. Silicon nitride tips with a nominal tip radius of 15 nm on a 0.1 N/m cantilever by Olympus (OMCL-RC800PSA) were used. Individual cantilevers were calibrated using thermal tuning.

## AFM image analysis

Both images and force curves were processed using home-built MATLAB software. Size and shape were analyzed from line profiles through the maximum of the vesicle along the slow scanning axis. Circular arcs were fitted to the part of the vesicle above half of the maximum height to obtain the radius of curvature, from which the tip radius (2 nm/15 nm, as provided by the manufacturer) was subtracted. The height of vesicles was derived from force-distance curves (FDCs), and the difference between the height obtained from FDCs and images was used for a subsequent correction of $R_c$ (49). $R_0$, the unperturbed vesicle radius in dispersion, was calculated under the assumption of surface area conservation as previously described (49).

## AFM FDC analysis

Analysis was done as described in detail previously (49). Briefly, raw data of a force cycle, given by the deflection of the cantilever versus the Z-piezo displacement, was converted to force versus separation (between the tip and the sample, or FDC) by subtracting the cantilever deflection. Contact point between tip and vesicle was found by using a change point algorithm and occasionally manually adjusted. Stiffness of the vesicles was found by fitting a straight line in the interval between 0.02 and 0.1 $R_c$. For finding the tether force, a step-fitting algorithm based on the change point analysis, which divides the curve into segments with slope 0, was used. Only adhesion events extending beyond the contact point were included. For fitting to the theory, described in detail elsewhere (49), the sum of the squared log Euclidian distance between the theoretical curve and the individual experimental data points was then minimized by adjusting $\kappa$ as a single fitting parameter. Confidence intervals were estimated using the bias-corrected percentile method with 1000 bootstrapping repetitions, for which a set of observed value combinations equal in size to the original data set was randomly drawn and fitted.

# RESULTS

## Membrane interactions induced by Syt1-$C_2$AB are $Ca^{2+}$- and protein-concentration dependent

We probed membrane-membrane interactions induced by Syt1-$C_2$AB using a combination of optical tweezers and confocal fluorescence microscopy. Two microspheres (3.84 $\mu$m in diameter) coated with single phospholipid bilayers (PC:PS:cholesterol, 50:20:30, unless otherwise specified) were brought into contact by an automated approach and separation method, as previously described (Fig. 1 *a*; (46)). By monitoring the forces upon approach and retraction of the beads in the presence of proteins, we can 1) detect the presence of tethers from the change in force (see event 3 in Fig. 1 *a* and force-time plot in Fig, 1 b); 2) quantify the tether strength, which is the force at which the beads become disconnected upon membrane pulling (rupture force, Fig. 1 *b*); and 3) visualize, using confocal microscopy, single tethers in the presence of labeled proteins (Syt1-$C_2$AB-mCherry, Fig.1 *c*, top panel) or labeled phospholipids (1% Rhodamine-PE, Fig. 1 *c,* bottom panel).

To use this approach for studying $C_2$AB-membrane interactions, we first established that the observed membrane tethers were Syt1-$C_2$AB-dependent (Figs. 2 and S1). By increasing the $Ca^{2+}$ concentration in the presence of 0.2 $\mu$M Syt1-$C_2$AB in solution, the probability of interactions increased from 40% at 100 $\mu$M $Ca^{2+}$ to 83% at 500 $\mu$M $Ca^{2+}$ (Fig. 2 *a*). In the absence of protein, the probability of tether formation was lower than 3% at any of the $Ca^{2+}$ concentrations tested (Fig. 2 *a*). The normalized cumulative distributions of the tether rupture forces (Fig. 2 *b*, inset) and the median of these distributions (i.e., the forces at which half of the observed interactions break; Fig. 2 *b*) reveal that the tether strength is approximately proportional to the $Ca^{2+}$ concentration. Furthermore, the probability of interactions (Fig. 2 *c*) and the median rupture forces (Fig. 2 *d*) at constant $Ca^{2+}$ concentration (500 $\mu$M) increased as a function of the protein concentration. These results demonstrate that our method is suitable for detecting $C_2$AB-specific interactions.

## Optimal membrane bridging

To investigate how the membrane binding activity described above is supported by different protein-membrane binding

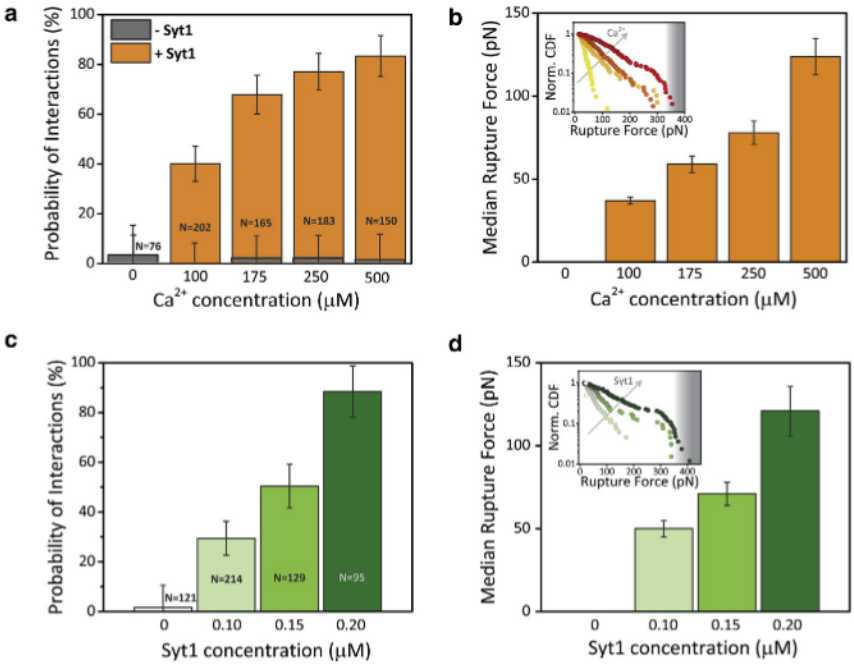


FIGURE 2 Membrane interactions induced by Syt1-$C_2$AB are dependent on $Ca^{2+}$ and protein concentration. (*a*) Shown is the probability of membrane interactions with increasing $Ca^{2+}$ concentration (in the absence of proteins or presence of 0.2 $\mu$M Syt1-$C_2$AB, *gray* and *orange histogram*, respectively). Numbers of approach and separation cycles (*N*) are indicated. At least 10 bead pairs were measured for each sample, with 10 cycles for each bead pair. Error bars indicate statistical error. (*b*) Median tether rupture forces at different $Ca^{2+}$ concentrations are shown. Inset: shown are normalized cumulative distribution functions (CDF) of the rupture forces (*color-coded* from *yellow* to *red* as the $Ca^{2+}$ increases) from which the median forces are calculated. (*c*) Shown is the probability of membrane interactions with increasing Syt1-$C_2$AB concentration (at fixed 0.5 mM $CaCl_2$). Numbers of interactions (*N*) are indicated. Error bars are statistical error. (*d*) Shown are median rupture forces with increasing Syt1-$C_2$AB concentration. Inset: normalized CDF of the rupture forces recorded (*color-coded* from *light* to *dark green* as the Syt1 concentration increases). In (*b*) and (*d*), the gray background gradient marks the maximum force that can be determined with the optical trap at the set laser power (5 W) and bead size (3.84 $\mu$m diameter). Error bars in rupture force plots indicate the standard deviation of the bootstrapped median rupture force values. The Kolmogorov-Smirnov test for all data both for (*b*) and (*d*) shows significantly different distribution at the $p < 0.0005$ level. To see this figure in color, go online.

modes, we employed two experimental arrangements, which are called "symmetric" and "asymmetric." In the asymmetric configuration, illustrated in Fig. 3 *a*, upper panel, the proteins were only bound on one membrane-coated microsphere and brought into contact with a protein-free membrane on the other microsphere. In the symmetric case, proteins were bound to both membranes, as shown schematically in Fig. 3 *a* (bottom panel) and visualized with fluorescence in Fig. 1 *c*. The confocal imaging confirms that, in the asymmetric configuration, Syt1-$C_2$AB-mCherry remained bound only to a single membrane-coated microsphere, suggesting that protein redistribution by membrane dissociation and reassociation was minimal over the time course of the experiment. Syt1-$C_2$AB-mCherry was also present on a tether that extended from the protein-coated bead (fluorescence image Fig. 3 *a*, middle panel, and Fig. S2). This tether configuration, i.e., extension from one of the beads, was also observed in symmetric protein configurations with a single phospholipid-labeled bead (Fig. S2). We note that all force measurements presented in this manuscript were obtained with unlabeled proteins, whereas mCherry Syt1 was only used for imaging. As shown in Fig. 3 *b*, Syt1-$C_2$AB was more effective in the asymmetric configuration, resulting in a more than 2-fold-higher probability of interactions and 3-fold-stronger tethers (Fig. 3 *b*). This behavior was consistent at different Syt1 concentrations, as shown in Fig. S1, which also demonstrates that the protein was not saturated under these conditions. Our liposome aggregation assay provides further evidence that the protein concentrations used throughout the optical tweezers experiments are below the saturation limit, as shown in Fig. S3. Performing the same experiments with Doc2b revealed the opposite behavior: the probability of interactions and rupture forces were strongly enhanced in the symmetric configuration (Fig. 3 c). Here, a concentration of 0.05 $\mu$M was used for Doc2b because at higher protein concentrations, the strong tethers that formed exceeded the instrument force limitation at our experimental conditions.

Statistical significance of the results was determined by a two-sample Kolmogorov-Smirnov test. This is a two-tailed non-parametric test that quantifies the distance between the empirical distributions of two data sets, in which the null hypothesis states that the two samples are drawn from the same distribution. Rupture forces in symmetrical versus asymmetrical configurations were found to be significantly different for both Syt1 and Doc2b, with $p < 0.05$. Note that the concentration used for Doc2b is comparable to the lowest concentration used for Syt1 in Fig. S1 and, hence, the difference in the preference for symmetry or asymmetry is unlikely to arise from the difference in concentration. The distinct results obtained with the two proteins also do not appear to arise from differences in their membrane affinities, because measurements of liposome aggregation as a function of protein concentration yielded similar EC50 values for the two proteins (Fig. S3). The activity of Syt1-$C_2$AB showed an optimum at 0.8 $\mu$M in the liposome aggregation assay. The reduced clustering activity at higher Syt1

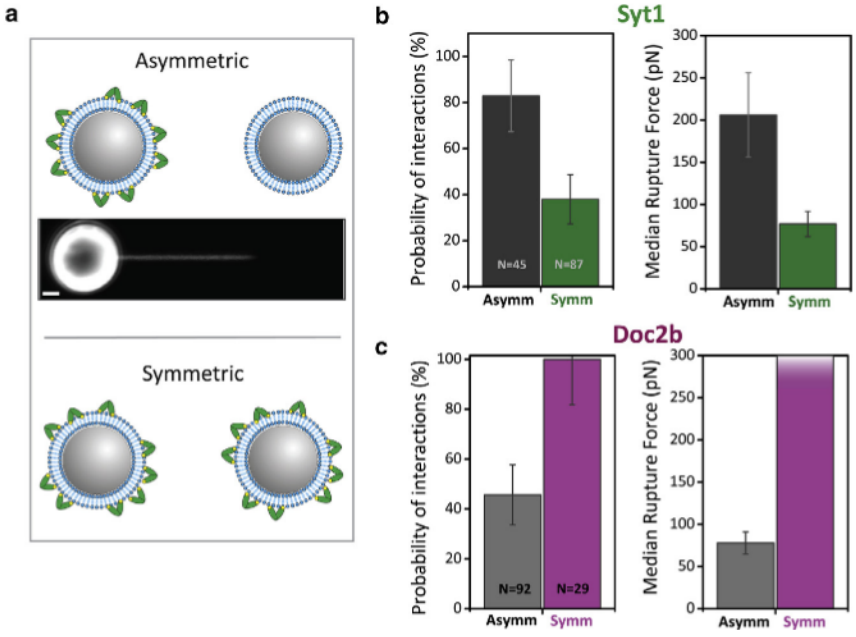


FIGURE 3 Optimal tethering by Syt1 and Doc2b loaded on single and dual membranes, respectively. (*a*) Shown is a schematic of the two experimental configurations used. Asymmetric: protein was bound to a single membrane-coated bead (*upper panel*), as confirmed by confocal imaging in which Syt1-$C_2$AB-mCherry (0.5 $\mu$M Syt1, 0.25 mM $CaCl_2$) was bound to the left bead and decorated the tether structure but not the other bead. Note that at other times, the tether was drawn from the dark bead, and no bias of tether extension toward labeled lipids was observed. Symmetric: proteins were bound to both beads (*bottom panel*, see Fig 1 *c* for confocal image). Scale bars, 1 $\mu$m. (*b*) Left: probability of Syt1-mediated membrane interactions in the asymmetric (*dark gray*) and symmetric (*green*) configurations. Error bars indicate statistical error. Right: median rupture force in the two configurations is shown. (*c*) Left: probability of Doc2b-mediated membrane interactions in the asymmetric (*light gray*) and symmetric (*magenta*) configurations is shown (0.05 $\mu$M Doc2b, 0.25 mM $CaCl_2$). Error bars are statistical error. Right: the median rupture force in the two configurations is shown. The color gradient in the symmetric configuration indicates a lower limit of this quantification because it reached the upper limit of our trapping force. Error bars indicate standard deviation of the bootstrapped median rupture force values. Note: the lower concentration of Doc2b compared with Syt1 is chosen to be within the range of break forces that can be experimentally quantified. To see this figure in color, go online.

concentrations may be due to prevalence of symmetric (protein-protein) interactions under such conditions.

## The impact of lipid composition

The presence of cholesterol is known to increase the efficiency of membrane fusion, likely by facilitating membrane curvature changes that lower the energy barrier for fusion (50,51). To explore the effect of cholesterol on $C_2$AB-mediated membrane-membrane interactions by Syt1 and Doc2b, we performed the same experiments in the presence or absence of cholesterol (PC:PS, 80:20, and PC:PS:cholesterol, 50:20:30). We tested the two $Ca^{2+}$ sensors in their most efficient configurations (i.e., asymmetric for Syt1 and symmetric for Doc2b). The probability of interactions did not increase further for Syt1-$C_2$AB (Fig. 4 *a*, panel i), but an increase in the median rupture force was observed (Fig. 4 *a*, right panel). In the case of Doc2b, cholesterol significantly increased both the probability of interactions and the tether strength (Fig. 4 *b*, cumulative distribution functions for the data presented in Fig. S4 are shown in Fig. S5). Statistical significance of the results was determined by a two-sample Kolmogorov-Smirnov test. Using this test to compare the distributions of tether break forces with and without added cholesterol in the membrane, we find that the difference for Doc2b- and Syt1-mediated tether break forces is statistically significant, with $p < 0.005$.

In addition to cholesterol, another lipid that is believed to be involved in Syt1 activity is $PIP_2$. It has been reported to play a role in determining binding specificity (6,15) as well as decreasing the rate of dissociation of Syt1 from the membrane while also enhancing membrane penetration (15). In addition, it was reported to lead to preferential association of the Syt1 $C_2$B domain with the plasma membrane in the low $Ca^{2+}$ state before fusion (and not with the vesicle membrane) (52). We therefore examined the effect of 1% $PIP_2$ addition on the strength and probability of interactions in our system, Fig. 5. $PIP_2$ appeared to increase the probability of interactions and the rupture force, but these effects did not reach statistical significance. These results are not surprising, because $PIP_2$ is known to considerably increase $Ca^{2+}$-independent membrane binding (6), but $Ca^{2+}$-dependent binding of Syt1-$C_2$AB to PS-containing membranes is very strong even in the absence of $PIP_2$, and the effects of Syt1 mutations on this activity correlate very well with their effects on neurotransmitter release in neurons (53,54). Thus, although $PIP_2$ binding to Syt1 is likely to be functionally important before $Ca^{2+}$ influx, it may not be crucial for $Ca^{2+}$ triggering, and the effects of $PIP_2$ on $Ca^{2+}$-dependent membrane binding are likely too small to have major effects on the measurements of Fig. 5.

## Syt1 and Doc2b can form different membrane tethers

To understand the membrane configuration in the tether structure, we used confocal fluorescent microscopy to differentiate between protein-mediated membrane bridging and hemifusion events. To this end, one of the trapped beads was labeled with a fluorescent phospholipid tracer (PC:PS:Rhodamine-PE, 79:20:1, or PC:PS:cholesterol:Rhodamine-PE,

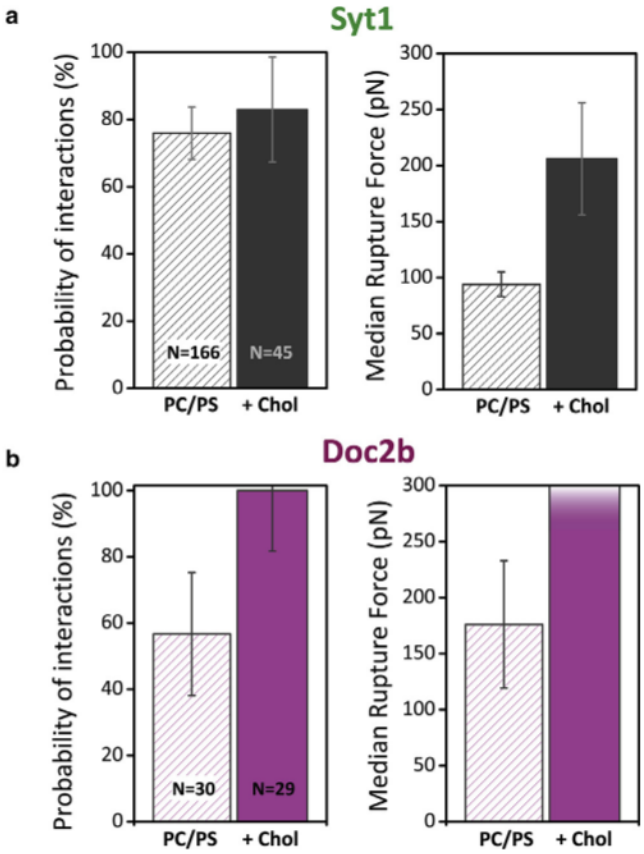


FIGURE 4 Cholesterol significantly increases strength and probability for Doc2b-mediated tethers. Probability of interactions and median rupture forces for membranes containing only PC/PS (80:20) and in the presence of cholesterol (30%, +Chol). (*a*) Shown are Syt1-mediated interactions tested in the asymmetric configuration (0.5 $\mu$M, 0.25 mM $CaCl_2$). (*b*) Shown are Doc2b-mediated interactions tested in the symmetric configuration (0.05 $\mu$M, 0.25 mM $CaCl_2$). Numbers of approach and separation cycles (*N*) are indicated. Error bars in probability plots indicate statistical error; error bars in rupture force plots indicate standard deviations of the bootstrapped median rupture force values. Tether break forces with and without added cholesterol in the membrane are significantly different for both Doc2b- and Syt1, with $p < 0.005$. To see this figure in color, go online.

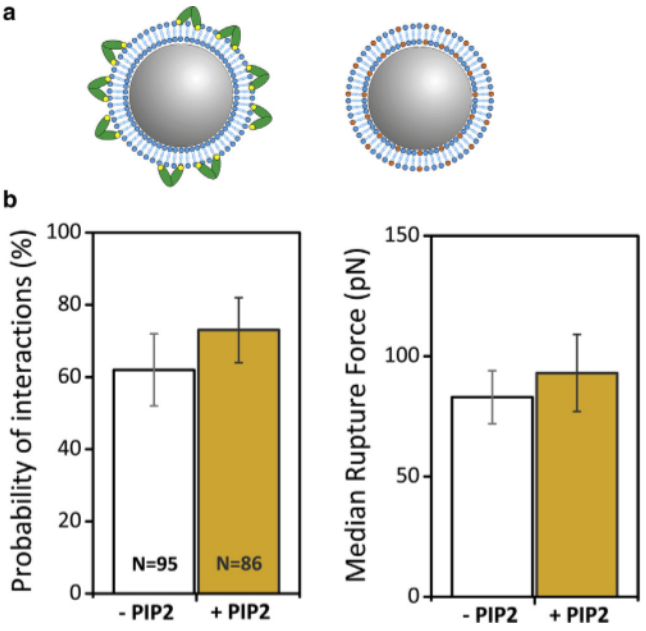


FIGURE 5 Membrane interactions in the presence of PI(4,5)P2. (*a*) Shown is a schematic illustration of the experimental configurations used: Syt1-$C_2$AB-mCherry (0.5 $\mu$M Syt1, 0.25 mM $CaCl_2$) was bound to a single membrane-coated PC/PS (80:20) bead (*left*); the opposite bead was coated with an additional 1% $PIP_2$, and it was left protein-free (*right bead*) (+$PIP_2$ configuration). We compare this configuration with the same asymmetric setting but in the absence of $PIP_2$ from both membrane-coated beads (−$PIP_2$ configuration). (*b*) Left plot: shown is the probability of Syt1-mediated membrane interactions in the absence of $PIP_2$ (*white bar*) and in the presence of $PIP_2$ (as schematically depicted in (*a*), *orange bar*). Error bars indicate statistical error. Right plot: median rupture force in the two configurations. Error bars indicate standard deviations of the bootstrapped median rupture force values. A Kolmogorov-Smirnov test showed no statistically significant difference at $p < 0.05$. To see this figure in color, go online.

49:20:30:1), whereas the other bead was unlabeled (PC:PS, 80:20, or PC:PS:cholesterol, 50:20:30). The beads were brought into contact and separated to a distance of 200–300 nm in the presence of Syt1 or Doc2b with the whole process of approach, waiting in contact and separation to a small distance lasting ~10 s. Once tether formation was measured as a force increase, continuous confocal imaging was used to monitor the fluorescence of the dark bead. If hemifusion occurs, phospholipid mixing is expected to cause a fluorescence increase in the outer leaflet of the dark bead (see the schematic in Fig. 6 *a*). The same method was previously used to demonstrate that Doc2b can induce hemifusion, whereas lack of full fusion is evident from a lipid-mixing assay (46). (We cannot completely exclude the less likely possibility of lipid transfer mediated by the protein.) Typical images from such experiments are shown in Fig. 6 *b* for one bead pair in the presence of 0.5 $\mu$M Syt1 (green) showing no hemifusion, and one bead pair in the presence of Doc2b (magenta) at 0.7 $\mu$M showing hemifusion, as seen also from the corresponding fluorescence intensity for this bead pair in Fig. 6 *d*, in which the fluorescent signal of the dark bead increased markedly due to lipid mixing (see also the fluorescence intensity shift quantified in Fig. S7). This concentration, which is higher than the one used in Fig. 3, was experimentally chosen to obtain sufficiently frequent hemifusion events, as optimized in our previous study (46). To explore the conditions that allow hemifusion, we tested multiple bead pairs at different protein concentrations and different configurations (symmetric/asymmetric) as well as different lipid compositions (with/without cholesterol). These measurements are summarized in Fig. 6 *e*; for lower concentrations of Syt1-$C_2$AB (0.5 $\mu$M), no hemifusion occurred regardless of the presence of cholesterol and regardless of the symmetric or asymmetric configuration. However, at high Syt1-$C_2$AB concentrations, we observed a remarkable effect: although no hemifusion occurred in the symmetric configuration, the asymmetric configuration yielded hemifusion in 53% of the cases. Doc2b induced hemifusion already

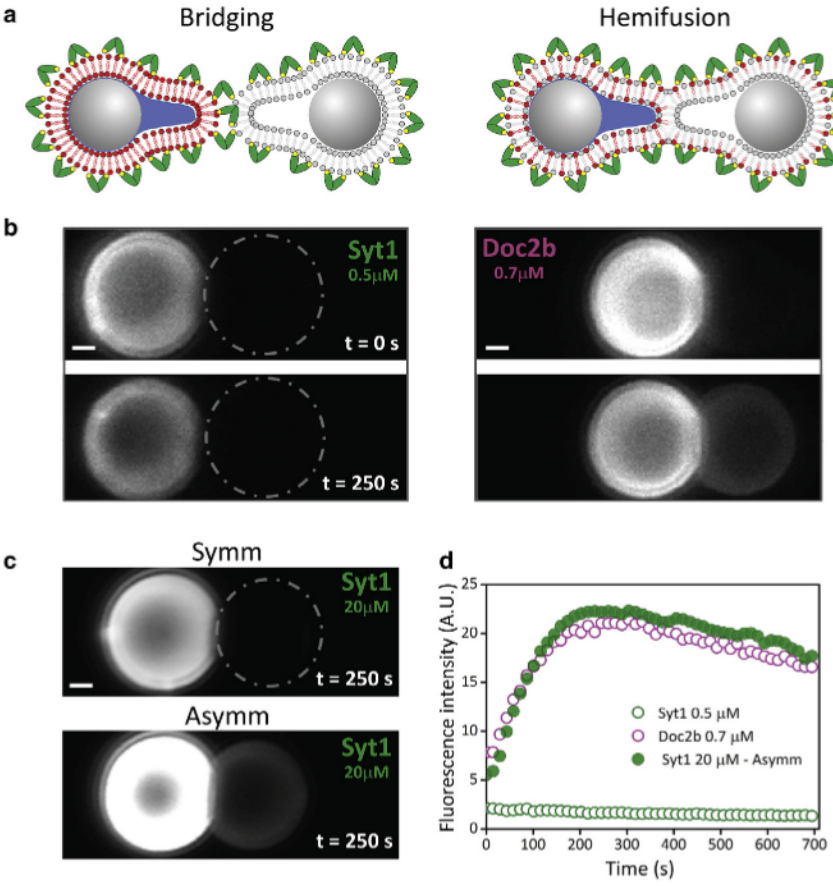


e

| | [μM] | Lipids | Configuration | Hemifusion probability (%) | # bead pairs |
|---|---|---|---|---|---|
| Syt1 | 0.5 | PC/PS | Asymm/Symm | 0 | 30 |
| | | + Chol | Asymm/Symm | 0 | 28 |
| | 20 | + Chol | Symm | 0 | 10 |
| | | + Chol | Asymm | 53 | 15 |
| Doc2b | 0.7 | PC/PS | Symm | 7 | 15 |
| | | + Chol | Symm | 48 | 27 |

FIGURE 6 Membrane bridging and hemifusion induced by Syt1 and Doc2b. (*a*) Shown is a schematic of possible protein-mediated membrane interactions (proteins bound on the membrane are represented in *green*). Left panel: shown are membranes bridging in which the bilayers stay separated and therefore labeled phospholipids (represented in *red*) remain on one membrane. Right panel: hemifusion is shown in which the proximal membrane leaflets have fused, causing lipid mixing. (*b*) Shown are confocal images in which only one membrane (*left bead*) was fluorescently labeled (1% Rhodamine-PE). Imaging was initiated as soon as a tether was detected. Upper panels: shown are images recorded at $t = 0$ s. Lower panels: shown are images recorded after 250 s. Shown are observed interactions mediated by Syt1 (*left panel*) and by Doc2b (*right panel*). (*c*) Shown are confocal images recorded after a 250-s interaction in the presence of 20 $\mu$M Syt1 in the symmetric (Symm) configuration (*upper panel*) and in the asymmetric (Asymm) configuration (*bottom panel*). (*d*) Shown is the fluorescence signal recorded from the dark bead over time in the presence of 0.7 $\mu$M Doc2b and 0.5 or 20 $\mu$M Syt1 in (*b*). (*e*) Shown are hemifusion probabilities under different conditions. To see this figure in color, go online.

at a lower concentration of 0.7 $\mu$M. These lipid-mixing experiments are limited by an experimental time window of around 10 min because of photobleaching. The observed intensity decrease between 300 and 700 s in Fig. 6 *d* is caused by such photobleaching. We conclude that the membrane tethers formed by Syt1-$C_2$AB typically represent proteolipid structures held together by membrane bridging unless a high concentration and asymmetric configuration are used, whereas Doc2b-induced tethers can represent either membrane-bridged or hemifused states.

## Doc2b and Syt1 reduce the membrane bending modulus

Several studies demonstrated that upon $Ca^{2+}$ binding, $C_2$AB domains insert into the lipid membrane (7,17). Such insertion is expected to induce membrane curvature (21,22). Because it disturbs the packing of the lipid acyl chains, this might result in a change in the mechanical properties of the membrane. In line with this, a recent model suggests that $Ca^{2+}$ binding and subsequent Syt1-membrane interaction results in local acyl chain disorder, which then drives a conformational change in the SNARE complex that results in fusion (24). To quantitatively study how Doc2b and Syt1 $C_2$AB fragment insertion into the negatively charged membrane influences its mechanical properties, we used a recently developed method based on AFM nanoindentation (49,55,56). By first imaging liposomes (Fig. 7 *a*) and then indenting them with the AFM tip, we can measure the membrane radius, stiffness, and membrane tension of single liposomes. These experimentally determined parameters are then fitted to a Helfrich-based model from which the

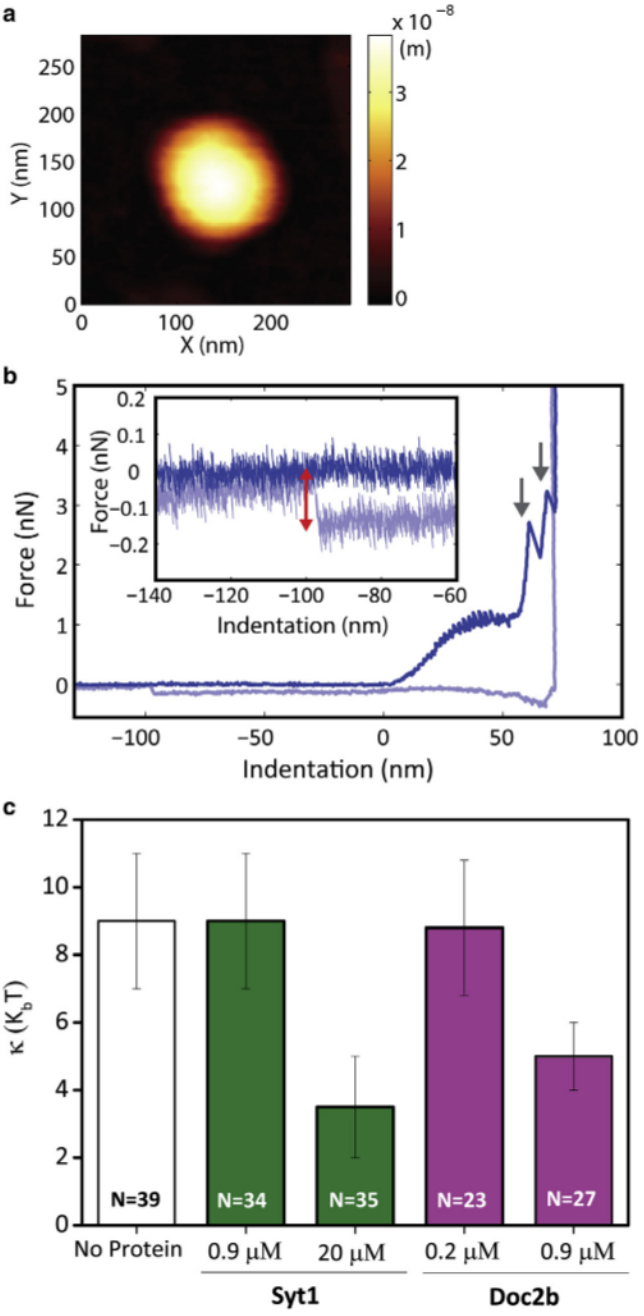


FIGURE 7 High concentrations (20 $\mu$M) of Syt1-$C_2$AB and lower concentrations (0.9 $\mu$M) of Doc2b-$C_2$AB reduce the membrane-bending modulus. (*a*) Shown is an AFM image of a typical vesicle: 44% cholesterol, 20% porcine brain PS, 21% egg PC, and 15% egg SM. (*b*) A typical force plot obtained by nanoindentation of a vesicle is shown. From the slope of the initial linear part, the stiffness of the vesicle is obtained. Two rupture events of the two bilayers can be observed, and a tether is formed upon tip retraction. Dark blue: approach; light blue: retraction. Inset: zoom in on the tether rupture force, which is used to calculate the osmotic pressure in the vesicle as described in Vorselen et al. (49). The red arrow shows the difference in force. (*c*) Bending modulus values for various concentrations of Syt1-$C_2$AB and Doc2b-$C_2$AB, with *N* values indicating the numbers of indented vesicles. Error bars mark 68% confidence intervals determined by bootstrapping. To see this figure in color, go online.

bending modulus is derived (49) (Fig. S6). A phospholipid composition of 44% cholesterol, 20% porcine brain PS, 21% egg PC, and 15% egg SM was chosen because it results in stable liposomes that do not rupture during the experiments. Although this is a high cholesterol content, it is well in line with the physiological lipid composition: the cholesterol-to-phospholipid ratio in synaptosomes varies between 0.5 and 1 (48). The extruded liposomes, with a 120 $\pm$ 30 nm average diameter (by dynamic light scattering (DLS)), were found to have a bending modulus $\kappa = 9 \pm 2$ $k_BT$. When performing the experiments in the presence of 0.9 $\mu$M Syt1, $\kappa = 9 \pm 2$ $k_BT$ was obtained, similar to the result in the absence of protein. In the presence of a high protein concentration (20 $\mu$M Syt1-$C_2$AB), which is in the same range as the concentration previously estimated by Western blot analysis of isolated synaptosomes (48) and the concentration when we observe hemifusion induced by Syt1, the bending modulus was reduced 3-fold (Fig. 7 *c*). When performing these experiments in the presence of Doc2b, the membrane bending modulus was unchanged at 0.2 $\mu$M protein concentration; however, a reduction in the bending modulus was observed already at 0.9 $\mu$M protein concentration. These results directly and quantitatively demonstrate that $C_2$AB domains have a mechanical effect on the membranes they attach to and that the extent of this effect varies between proteins.

## DISCUSSION

In this work, we observed that the $C_2$AB domain of Syt1 induces the formation of membrane tethers in a manner dependent on $Ca^{2+}$ and protein concentration. Similar to Doc2b-induced membrane tethers (46), Syt1-induced tethers contained both protein (shown by Syt1-$C_2$AB-mCherry labeling) and phospholipid (shown by Rhodamine-PE labeling) and resisted high forces during bead separation.

Our experiments, which were performed under cell-free conditions, highlight several important differences between Syt1- and Doc2b-induced membrane tethers. When comparing symmetrical (both sides) and asymmetrical (one side) presence of protein on the membranes, Syt1 favors an asymmetrical configuration, and Doc2b favors a symmetrical configuration. This difference is reminiscent of the physiological configuration of the two proteins: Syt1 is anchored to the vesicle membrane by a transmembrane domain, and Doc2b is a soluble protein that can diffuse in the cytoplasm and has access to both the vesicle and target membranes (38–40,48,57,58). When expressed as a Doc2b-EGFP fusion, the fluorescence is usually homogeneously distributed in the cytosol and accumulates with the plasma membrane in a $Ca^{2+}$-dependent manner. Using subcellular fractionation and Western blotting, Doc2b was also observed in the synaptic vesicle fraction (Fig. 3; (57)) therein, although a direct comparison between the Doc2b

distribution in vivo and the membrane-bound configuration in our experimental setup is complicated by differences in the free $Ca^{2+}$ concentration, membrane compositions, and absence of the Doc2b N-terminal domain, which contains a Munc13-binding site). For Syt1, two hypotheses pertaining to the mechanism of membrane bridging have been proposed (reviewed by Seven et al. (12)): the direct bridging hypothesis, which states that $C_2AB$ molecules bind simultaneously to both membranes, and the oligomerization hypothesis, in which interactions between $C_2AB$ oligomers formed on both membranes bridge the membrane gap. The higher activity of Syt1 in the asymmetric setup, which might favor protein-membrane interactions, seems to support the direct bridging hypothesis. This notion was confirmed by the lack of Syt1-mCherry redistribution to the unlabeled bead in our experiments. Doc2b, on the other hand, was more efficient in the symmetric conformation, which may suggest a preference for protein-protein (and not protein-membrane) interactions under our experimental conditions. Nevertheless, we cannot exclude the possibility that while acting on both membranes, Doc2b increases the probability for a lipid tether formation because of its effect on lipid packing without direct protein-protein interactions.

Another difference is observed in membrane bridging versus hemifusion. In confocal fluorescence microscopy of bead pairs, the ability of the fluorescent phospholipid tracer Rhodamine-PE to diffuse to an unlabeled bead was used to discriminate between two possible membrane configurations: structures without membrane continuity (likely resulting from membrane bridging) and structures with membrane continuity (likely representing hemi(fused) membranes, as observed previously) (12). For lower concentrations of Syt1-$C_2AB$, all 58 membrane tethers examined in our study appeared to originate from membrane bridging. This result is consistent with previous studies that demonstrated membrane bridging by Syt1 (11,12) at similar concentrations. At 20 $\mu$M protein concentration, Syt1 induced hemifusion in the presence of cholesterol and only in the asymmetrical configuration. In contrast, Doc2b-induced membrane tethers resulted in both membrane-bridged and hemifused structures already at lower protein concentrations.

Although the estimated in vivo concentration is 70 $\mu$M (46), a concentration of 20 $\mu$M is high with respect to the local lipid concentration and could thus cause molecular crowding at the membrane surface. In addition, Syt1 can engage in several other interactions in vivo. Thus, although our observation of hemifusion for a $Ca^{2+}$ sensor protein implicated in membrane fusion triggering is of high interest, it should be further tested in living neurons. In general, the strength of our in vitro approach is that we can focus on a limited set of variables and that the exact composition of the system is a priori known. This is very helpful to discern the effect of specific variables. However, our single-particle experiments have certain limitations as to minimum and maximum protein concentrations that can be used, and this should be borne in mind with regard to the biological significance.

When comparing tether rupture forces, several factors need to be taken into account. The rupture is expected to occur at the weakest point, which is most likely at the contact between the membranes. The contact point can either be composed of membrane-bound protein (bridging), a continuous outer membrane leaflet (hemifusion), or a fully fused membrane (which has been excluded in content mixing experiments (46)). For Doc2b- and Syt1-generated membrane tethers, the rupture force was increased in the presence of 30% cholesterol, a lipid that has been suggested to assist membrane fusion (50). Because of its effective negative curvature, cholesterol has been proposed to lower the energy for forming lipid hemifusion stalks that are thought to be intermediates in membrane fusion (59,60). As for Doc2b, the dramatic increase in rupture force beyond the measurement limit correlates with the increase in hemifusion observed in our confocal fluorescence measurements, and we hypothesize that upon hemifusion, stronger tethers will be formed. Possibly, such strong tethers are not ruptured in our experiments because the maximal forces we can apply are limited by the optical trapping power. For Syt1-$C_2AB$-induced tethers, the median rupture force most likely represents protein-membrane interactions with a median rupture force in the 50–200 pN range, strongly dependent on the $Ca^{2+}$ (which regulates $C_2AB$-membrane binding) and protein concentration. The binding force of one Syt1 molecule to a membrane is in the range of several piconewtons (61). Therefore, the differences we observe in the force probably relate to a variation in the number of bound molecules at the contact site.

Membrane fusion is energetically unfavorable and necessitates crossing of several energy barriers (62). One major energy barrier is associated with the strong repulsive hydration forces between bilayers. Other energy-costly intermediates include lipid splaying during initiation of hemifusion-stalk formation, stalk expansion, which yields the hemifusion diaphragm, and finally, fusion pore formation and its expansion (63). In the case of synaptic vesicle fusion, the activation energy of bilayer-bilayer fusion is very high ($\sim$40 $k_BT$), and the process is aided by important proteins, including SNAREs, complexin, and $Ca^{2+}$ sensors. It has been suggested that in response to $Ca^{2+}$ binding, Syt1 could promote SNARE-mediated fusion by lowering this energy barrier via induction of positive curvature in target membranes upon insertion of $C_2$ domains into the membrane (22). Using AFM, we have directly measured a significant reduction in the bending modulus of a lipid membrane upon Syt1-$C_2AB$ binding (Fig. 7) in the presence of 20 $\mu$M protein, which is possibly related to this membrane-insertion of $C_2$ domains. For Doc2b, a significant reduction of the bending modulus was observed already at 0.9 $\mu$M protein concentration. This difference could be due to larger

effective curvature for Doc2b, which is expected to decrease membrane thickness (64), thus affecting the bending modulus that depends on membrane thickness to the power of three (65). A membrane inclusion with higher curvature is theoretically predicted to result in a larger reduction in the bending modulus (66). How does this global change in the mechanical property of the membrane relate to the local event of hemi(fusion)? A possible explanation is that while mambrane thinning may occur globally, membrane "dimples" form locally because of protein insertion. The curvature induction hypothesis predicts the formation of a buckle-like membrane structure between protein insertions in the membrane. Locally, the end cap membrane is highly curved, and thus the lipids are under stress. This stress is partially relieved during lipid rearrangements accompanying the fusion process, which reduces the overall energy cost of the reaction, thus facilitating membrane fusion (21). We note that it is difficult to compare results of bending moduli obtained by different methods, as large variations exist in bending modulus values for the same bilayer composition obtained by different measurement techniques (67). Nonetheless, our results are in the same range as other reported values (68,69).

## CONCLUSIONS

Combining all observations, it is likely that membrane insertion of the $C_2$AB domain of Doc2b results in a larger disruption of the lipid packing compared with Syt1, consequently reducing the energy barrier for hemifusion and allowing hemifusion already at lower protein concentrations. Syt1, however, might not sufficiently disrupt membrane structure at lower concentrations, and changing the configuration to asymmetrical or adding cholesterol is not sufficient to push the membranes toward hemifusion. Only at higher concentrations, enough disruption to membrane packing is attained, manifested in lower bending modulus and, concomitantly, high hemifusion probability in the asymmetrical configuration. The lowering of the energy required for membrane deformation possibly contributes to the function of these and other $C_2$AB-containing $Ca^{2+}$ sensor proteins.

## SUPPORTING MATERIAL

Supporting Material can be found online at https://doi.org/10.1016/j.bpj.2019.12.021.

## AUTHOR CONTRIBUTIONS

R.S., M.M., A.J.G., and G.J.L.W. conceived and planned the experiments. R.S., M.M., E.L., M.C.P., E.K., R.V., and A.J.G. carried out the experiments and analyzed the data, G.B. wrote the code for data analysis. R.S., M.M., M.C.P., J.R., W.H.R., A.J.G., and G.J.L.W. wrote the manuscript. All authors provided critical feedback that shaped the research, analysis, and manuscript.

## ACKNOWLEDGMENTS

The authors thank Michael Kozlov for insightful discussions and Ineke Brouwer for useful discussions and technical advice.

R.S. acknowledges support through the Human Frontier Science Program (HFSP) postdoctoral fellowship LT000419/2015, as well as support through the Israeli National Postdoctoral Award for Advancing Women in Science and the L'Oreal UNESCO award for advancing women in science. W.H.R. acknowledges the support of the Nederlandse Organisatie voor Wetenschappelijk Onderzoek Vidi grant. J.R. acknowledges the support of the Welch Foundation (grant I-1304) and the National Institutes of Health (Research Project Award R35 NS097333).

## REFERENCES

1. Südhof, T. C. 2013. Neurotransmitter release: the last millisecond in the life of a synaptic vesicle. *Neuron.* 80:675–690.
2. Rizo, J. 2018. Mechanism of neurotransmitter release coming into focus. *Protein. Sci.* 27:1364–1391.
3. Zhou, Q., Y. Lai, …, A. T. Brunger. 2015. Architecture of the synaptotagmin-SNARE machinery for neuronal exocytosis. *Nature.* 525:62–67.
4. Zhou, Q., P. Zhou, …, A. T. Brunger. 2017. The primed SNARE-complexin-synaptotagmin complex for neuronal exocytosis. *Nature.* 548:420–425.
5. Brewer, K. D., T. Bacaj, …, J. Rizo. 2015. Dynamic binding mode of a Synaptotagmin-1-SNARE complex in solution. *Nat. Struct. Mol. Biol.* 22:555–564.
6. Bai, J., W. C. Tucker, and E. R. Chapman. 2004. $PIP_2$ increases the speed of response of synaptotagmin and steers its membrane-penetration activity toward the plasma membrane. *Nat. Struct. Mol. Biol.* 11:36–44.
7. Chapman, E. R. 2008. How does synaptotagmin trigger neurotransmitter release? *Annu. Rev. Biochem.* 77:615–641.
8. Park, Y., and J. K. Ryu. 2018. Models of synaptotagmin-1 to trigger $Ca^{2+}$ -dependent vesicle fusion. *FEBS Lett.* 592:3480–3492.
9. Südhof, T. C., and J. E. Rothman. 2009. Membrane fusion: grappling with SNARE and SM proteins. *Science.* 323:474–477.
10. van den Bogaart, G., S. Thutupalli, …, R. Jahn. 2011. Synaptotagmin-1 may be a distance regulator acting upstream of SNARE nucleation. *Nat. Struct. Mol. Biol.* 18:805–812.
11. Araç, D., X. Chen, …, J. Rizo. 2006. Close membrane-membrane proximity induced by Ca(2+)-dependent multivalent binding of synaptotagmin-1 to phospholipids. *Nat. Struct. Mol. Biol.* 13:209–217.
12. Seven, A. B., K. D. Brewer, …, J. Rizo. 2013. Prevalent mechanism of membrane bridging by synaptotagmin-1. *Proc. Natl. Acad. Sci. USA.* 110:E3243–E3252.
13. Rickman, C., D. A. Archer, …, B. Davletov. 2004. Synaptotagmin interaction with the syntaxin/SNAP-25 dimer is mediated by an evolutionarily conserved motif and is sensitive to inositol hexakisphosphate. *J. Biol. Chem.* 279:12574–12579.
14. van den Bogaart, G., K. Meyenberg, …, R. Jahn. 2011. Membrane protein sequestering by ionic protein-lipid interactions. *Nature.* 479:552–555.
15. Pérez-Lara, Á., A. Thapa, …, R. Jahn. 2016. $PtdInsP_2$ and PtdSer cooperate to trap synaptotagmin-1 to the plasma membrane in the presence of calcium. *eLife.* 5.
16. Kuo, W., D. Z. Herrick, and D. S. Cafiso. 2011. Phosphatidylinositol 4,5-bisphosphate alters synaptotagmin 1 membrane docking and drives opposing bilayers closer together. *Biochemistry.* 50:2633–2641.
17. Hui, E., J. Bai, and E. R. Chapman. 2006. Ca2+-triggered simultaneous membrane penetration of the tandem C2-domains of synaptotagmin I. *Biophys. J.* 91:1767–1777.

18. Rufener, E., A. A. Frazier, …, D. S. Cafiso. 2005. Membrane-bound orientation and position of the synaptotagmin $C_2B$ domain determined by site-directed spin labeling. *Biochemistry.* 44:18–28.

19. Frazier, A. A., C. R. Roller, …, D. S. Cafiso. 2003. Membrane-bound orientation and position of the synaptotagmin I $C_2A$ domain by site-directed spin labeling. *Biochemistry.* 42:96–105.

20. Herrick, D. Z., S. Sterbling, …, D. S. Cafiso. 2006. Position of synaptotagmin I at the membrane interface: cooperative interactions of tandem C2 domains. *Biochemistry.* 45:9668–9674.

21. McMahon, H. T., M. M. Kozlov, and S. Martens. 2010. Membrane curvature in synaptic vesicle fusion and beyond. *Cell.* 140:601–605.

22. Martens, S., M. M. Kozlov, and H. T. McMahon. 2007. How synaptotagmin promotes membrane fusion. *Science.* 316:1205–1208.

23. Hui, E., C. P. Johnson, …, E. R. Chapman. 2009. Synaptotagmin-mediated bending of the target membrane is a critical step in Ca(2+)-regulated fusion. *Cell.* 138:709–721.

24. Kiessling, V., A. J. B. Kreutzberger, …, L. K. Tamm. 2018. A molecular mechanism for calcium-mediated synaptotagmin-triggered exocytosis. *Nat. Struct. Mol. Biol.* 25:911–917.

25. Diao, J., P. Grob, …, A. T. Brunger. 2012. Synaptic proteins promote calcium-triggered fast transition from point contact to full fusion. *eLife.* 1:e00109.

26. Lai, Y., J. Diao, …, Y. K. Shin. 2013. Fusion pore formation and expansion induced by Ca2+ and synaptotagmin 1. *Proc. Natl. Acad. Sci. USA.* 110:1333–1338.

27. Wu, Z., L. Ma, …, E. Karatekin. 2018. Dilation of fusion pores by synaptotagmin-1 $C_2AB$ domains. *Biophys. J.* 114:282a.

28. Hui, E., J. D. Gaffaney, …, E. R. Chapman. 2011. Mechanism and function of synaptotagmin-mediated membrane apposition. *Nat. Struct. Mol. Biol.* 18:813–821.

29. Connell, E., A. Giniatullina, …, B. Davletov. 2008. Cross-linking of phospholipid membranes is a conserved property of calcium-sensitive synaptotagmins. *J. Mol. Biol.* 380:42–50.

30. Zanetti, M. N., O. D. Bello, …, S. S. Krishnakumar. 2016. Ring-like oligomers of Synaptotagmins and related C2 domain proteins. *eLife.* 5.

31. Wang, J., F. Li, …, J. E. Rothman. 2017. Circular oligomerization is an intrinsic property of synaptotagmin. *eLife.* 6.

32. Wang, J., O. Bello, …, J. E. Rothman. 2014. Calcium sensitive ring-like oligomers formed by synaptotagmin. *Proc. Natl. Acad. Sci. USA.* 111:13966–13971.

33. Caffrey, M., S. J. Morris, and G. W. Feigenson. 1987. Uranyl acetate induces gel phase formation in model lipid and biological membranes. *Biophys. J.* 52:501–505.

34. Groffen, A. J., S. Martens, …, M. Verhage. 2010. Doc2b is a high-affinity Ca2+ sensor for spontaneous neurotransmitter release. *Science.* 327:1614–1618.

35. Kojima, T., M. Fukuda, …, K. Mikoshiba. 1996. Calcium-dependent phospholipid binding to the $C_2A$ domain of a ubiquitous form of double C2 protein (Doc2 beta). *J. Biochem.* 120:671–676.

36. Giladi, M., L. Michaeli, …, J. A. Hirsch. 2013. The $C_2B$ domain is the primary Ca2+ sensor in DOC2B: a structural and functional analysis. *J. Mol. Biol.* 425:4629–4641.

37. Friedrich, R., A. J. Groffen, …, U. Ashery. 2008. DOC2B acts as a calcium switch and enhances vesicle fusion. *J. Neurosci.* 28:6794–6806.

38. Groffen, A. J., E. C. Brian, …, M. Verhage. 2004. Ca(2+)-induced recruitment of the secretory vesicle protein DOC2B to the target membrane. *J. Biol. Chem.* 279:23740–23747.

39. Duncan, R. R., A. Betz, …, R. H. Chow. 1999. Transient, phorbol ester-induced DOC2-Munc13 interactions in vivo. *J. Biol. Chem.* 274:27347–27350.

40. Groffen, A. J., R. Friedrich, …, M. Verhage. 2006. DOC2A and DOC2B are sensors for neuronal activity with unique calcium-dependent and kinetic properties. *J. Neurochem.* 97:818–833.

41. Geppert, M., Y. Goda, …, T. C. Südhof. 1994. Synaptotagmin I: a major Ca2+ sensor for transmitter release at a central synapse. *Cell.* 79:717–727.

42. Houy, S., A. J. Groffen, …, J. B. Sørensen. 2017. Doc2B acts as a calcium sensor for vesicle priming requiring synaptotagmin-1, Munc13-2 and SNAREs. *eLife.* 6.

43. Ramalingam, L., E. Oh, …, D. C. Thurmond. 2012. Doc2b is a key effector of insulin secretion and skeletal muscle insulin sensitivity. *Diabetes.* 61:2424–2432.

44. Yu, H., S. S. Rathore, …, J. Shen. 2013. Doc2b promotes GLUT4 exocytosis by activating the SNARE-mediated fusion reaction in a calcium- and membrane bending-dependent manner. *Mol. Biol. Cell.* 24:1176–1184.

45. Zhang, J., E. Oh, …, D. C. Thurmond. 2019. DOC2B promotes insulin sensitivity in mice via a novel KLC1-dependent mechanism in skeletal muscle. *Diabetologia.* 62:845–859.

46. Brouwer, I., A. Giniatullina, …, A. J. Groffen. 2015. Direct quantitative detection of Doc2b-induced hemifusion in optically trapped membranes. *Nat. Commun.* 6:8387.

47. Ubach, J., Y. Lao, …, J. Rizo. 2001. The $C_2B$ domain of synaptotagmin I is a Ca2+-binding module. *Biochemistry.* 40:5854–5860.

48. Wilhelm, B. G., S. Mandad, …, S. O. Rizzoli. 2014. Composition of isolated synaptic boutons reveals the amounts of vesicle trafficking proteins. *Science.* 344:1023–1028.

49. Vorselen, D., F. C. MacKintosh, …, G. J. Wuite. 2017. Competition between bending and internal pressure governs the mechanics of fluid nanovesicles. *ACS Nano.* 11:2628–2636.

50. Yang, S. T., A. J. B. Kreutzberger, …, L. K. Tamm. 2016. The role of cholesterol in membrane fusion. *Chem. Phys. Lipids.* 199:136–143.

51. Pan, J., S. Tristram-Nagle, and J. F. Nagle. 2009. Effect of cholesterol on structural and mechanical properties of membranes depends on lipid chain saturation. *Phys. Rev. E Stat. Nonlin. Soft Matter Phys.* 80:021931.

52. Nyenhuis, S. B., A. Thapa, and D. S. Cafiso. 2019. Phosphatidylinositol 4,5 bisphosphate controls the cis and trans interactions of synaptotagmin 1. *Biophys. J.* 117:247–257.

53. Fernández-Chacón, R., A. Königstorfer, …, T. C. Südhof. 2001. Synaptotagmin I functions as a calcium regulator of release probability. *Nature.* 410:41–49.

54. Rhee, J. S., L. Y. Li, …, C. Rosenmund. 2005. Augmenting neurotransmitter release by enhancing the apparent Ca2+ affinity of synaptotagmin 1. *Proc. Natl. Acad. Sci. USA.* 102:18664–18669.

55. Sorkin, R., R. Huisjes, …, G. J. L. Wuite. 2018. Nanomechanics of extracellular vesicles reveals vesiculation pathways. *Small.* 14:e1801650.

56. Vorselen, D., S. M. van Dommelen, …, W. H. Roos. 2018. The fluid membrane determines mechanics of erythrocyte extracellular vesicles and is softened in hereditary spherocytosis. *Nat. Commun.* 9:4960.

57. Verhage, M., K. J. de Vries, …, T. C. Südhof. 1997. DOC2 proteins in rat brain: complementary distribution and proposed function as vesicular adapter proteins in early stages of secretion. *Neuron.* 18:453–461.

58. Takamori, S., M. Holt, …, R. Jahn. 2006. Molecular anatomy of a trafficking organelle. *Cell.* 127:831–846.

59. Churchward, M. A., T. Rogasevskaia, …, J. R. Coorssen. 2008. Specific lipids supply critical negative spontaneous curvature–an essential component of native Ca2+-triggered membrane fusion. *Biophys. J.* 94:3976–3986.

60. Churchward, M. A., T. Rogasevskaia, …, J. R. Coorssen. 2005. Cholesterol facilitates the native mechanism of Ca2+-triggered membrane fusion. *J. Cell Sci.* 118:4833–4848.

61. Ma, L., Y. Cai, …, Y. Zhang. 2017. Single-molecule force spectroscopy of protein-membrane interactions. *eLife.* 6:e30493.

62. Clarke, S. 1981. The hydrophobic effect: formation of Micelles and biological membranes, 2nd edition (Tanford, Charles). *J. Chem. Educ.* 58:A246.

63. Chernomordik, L. V., and M. M. Kozlov. 2008. Mechanics of membrane fusion. *Nat. Struct. Mol. Biol.* 15:675–683.

64. Campelo, F., H. T. McMahon, and M. M. Kozlov. 2008. The hydrophobic insertion mechanism of membrane curvature generation by proteins. *Biophys. J.* 95:2325–2339.

65. Zimmerberg, J., and M. M. Kozlov. 2006. How proteins produce cellular membrane curvature. *Nat. Rev. Mol. Cell Biol.* 7:9–19.

66. Kozlov, M. M., and W. Helfrich. 1992. Effects of a cosurfactant on the stretching and bending elasticities of a surfactant monolayer. *Langmuir.* 8:2792–2797.

67. Nagle, J. F., M. S. Jablin, …, K. Akabori. 2015. What are the true values of the bending modulus of simple lipid bilayers? *Chem. Phys. Lipids.* 185:3–10.

68. Park, Y., C. A. Best, …, G. Popescu. 2010. Measurement of red blood cell mechanics during morphological changes. *Proc. Natl. Acad. Sci. USA.* 107:6731–6736.

69. Zhelev, D. V., D. Needham, and R. M. Hochmuth. 1994. A novel micropipet method for measuring the bending modulus of vesicle membranes. *Biophys. J.* 67:720–727.